

Received 14 October 2023; accepted 21 November 2023. Date of publication 28 November 2023; date of current version 19 December 2023.
The review of this article was arranged by Editor S. Menzel.

Digital Object Identifier 10.1109/JEDS.2023.3336077

A Kinetic Pathway to Orthorhombic $\text{Hf}_{0.5}\text{Zr}_{0.5}\text{O}_2$

**GUAN-HUA CHEN^{ID} 1 (Associate Member, IEEE), YU-RUI CHEN^{ID} 2 (Graduate Student Member, IEEE),
ZEFU ZHAO^{ID} 2 (Graduate Student Member, IEEE), JIA-YANG LEE³ (Graduate Student Member, IEEE),
YUN-WEN CHEN², YIFAN XING^{ID} 2 (Member, IEEE), RACHIT DOBHAL³ (Graduate Student Member, IEEE),
AND C. W. LIU^{ID} 1,2,3,4 (Fellow, IEEE)**

1 Graduate Institute of Photonics and Optoelectronics, National Taiwan University, Taipei 10617, Taiwan

2 Graduate Institute of Electronics Engineering, National Taiwan University, Taipei 10617, Taiwan

3 Graduate School of Advanced Technology, National Taiwan University, Taipei 10617, Taiwan

4 Department of Electrical Engineering, National Taiwan University, Taipei 10617, Taiwan

CORRESPONDING AUTHOR: C. W. LIU (e-mail: cliu@ntu.edu.tw; chee@cc.ee.ntu.edu.tw)

This work was supported in part by the National Science and Technology Council, Taiwan, under Grant NSTC 112-2218-E-002-024-MBK, and Grant 111-2634-F-A49-008; in part by the "Center for Advanced Semiconductor Technology Research" from The Featured Areas Research Center Program within the framework of the Higher Education Sprout Project by the Ministry of Education (MOE) in Taiwan; and in part by the Powerchip Semiconductor Manufacturing Corporation.

ABSTRACT To improve the crystallinity and phase composition of the $\text{Hf}_{0.5}\text{Zr}_{0.5}\text{O}_2$ films, the effects of annealing temperature on metal-ferroelectric-metal devices are studied by electrical measurements, nanobeam electron diffraction (NBD), and TEM. Forming gas annealing (FGA) at 400°C partially crystallizes the films, and more crystallization can be achieved by FGA at the increasing temperature of 500°C and 800°C. After FGA at 400°C and 500°C, metastable ferroelectric orthorhombic phase can be obtained as shown by electrical measurements and NBD. By the density functional theory (DFT) simulation, we propose that o-phase formation happens during both the annealing step as well as the cooling step. During the FGA at 800°C, the metastable orthorhombic phase overcomes the activation barrier and transforms into stable monoclinic phase. In this work, the systematic experimental study of phase transformation, free energy simulation for different phases, and schematic diagrams of free energy for phase transition at different temperatures are reported.

INDEX TERMS Ferroelectric (FE), $\text{Hf}_{0.5}\text{Zr}_{0.5}\text{O}_2$, nanobeam electron diffraction (NBD).

I. INTRODUCTION

Ferroelectric (FE) based non-volatile memories are demonstrated with favorable scalability and low power consumption [1]. Hafnium zirconium oxide (HZO) is the promising material of choice due to its CMOS process compatibility, large coercive field, and robust ferroelectric properties even in films lower than 10nm thick [2]. The ferroelectric memories, including ferroelectric random-access memories (FeRAM) [3], ferroelectric field effect transistors (FeFET) [4], and ferroelectric tunneling junctions (FTJ) [5] can be used to store data by retaining remanent polarization (P_r) even without applied voltage [6]. Since the ferroelectric properties come from the formation of orthorhombic phase (o-phase) in the HZO film [6], the ability to identify the o-phase crystal is critical for developing ferroelectric memories. However, it is reported that identifying the

o-phase crystal with grazing-incidence X-ray diffraction (GIXRD) is challenging because o-phase and tetragonal phase (t-phase) possess similar crystal structures and lattice constants [7], [8].

In this work, electrical measurements and nanobeam electron diffraction (NBD) were used to identify existence of o-phase. Relative free energies by the density functional theory (DFT) can explain the resulting phase distribution. For films annealed at 400°C and 500°C, the o-phase crystal can be identified by ferroelectric behavior in electrical measurements and bright spots in the NBD pattern. The DFT simulation shows that when considering bulk energy, entropy effects, and interfacial energy, o-phase has lower free energy than t-phase at 400°C and 500°C. And at room temperature, the free energy disparity between t-phase and o-phase increases. This indicates that o-phase formation

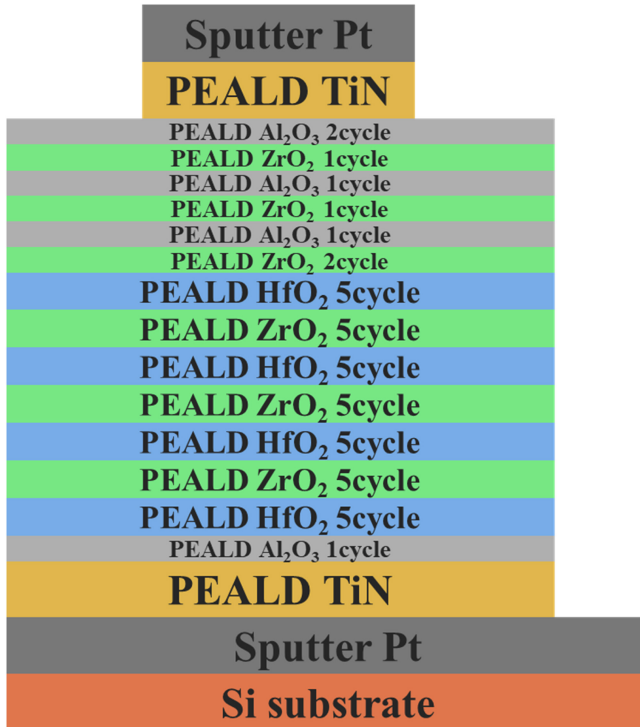


FIGURE 1. Schematic of sputtered Pt/PEALD TiN/PEALD H5Z5 (4 periods) + A1Z1(3 periods) /PEALD TiN/sputtered Pt stacks.

happens when the as-deposited amorphous HZO layer crystallizes during the annealing step. t-phase also transforms into o-phase during the cooling step because the activation barrier for transforming from t-phase to o-phase lowers as the temperature drops, as previously reported [9]. A schematic landscape of free energy is proposed to illustrate the annealing and cooling effect to increase the o-phase. At 400°C and 500°C, the o-/t-phase crystal doesn't have enough thermal energy to cross the barrier between metastable o-/t-phase and stable m-phase, resulting in ferroelectric films after cooling. For FGA at 800°C, NBD spots resembling m-phase are the only observable spots despite the high-crystalline of the HZO layer. As the annealing temperature increase to 800°C, the metastable o-/t-phase receives enough thermal energy to overcome the activation barrier and transformed into stable m-phase.

II. EXPERIMENTS

Pt/TiN/Al₂O₃/Hf_{0.5}Zr_{0.5}O₂/Al₂O₃-ZrO₂/TiN/Pt films were grown on Si substrates (Figure 1). The device was fabricated by first sputtering the Pt bottom probe layer, followed by plasma-enhanced atomic layer deposition (PEALD) of TiN/Al₂O₃/Hf_{0.5}Zr_{0.5}O₂/Al₂O₃-ZrO₂/TiN layers. Precursors of HfO₂, ZrO₂, Al₂O₃, and TiN were TDMAH, TDMAZ, TMA, and TDMAT, respectively. 30 sec of O₂ plasma was used as the oxidant for Hf_{0.5}Zr_{0.5}O₂ and Al₂O₃-ZrO₂ layers. TiN was used as the bottom electrode and the top electrode. The TiN bottom electrode was treated with in-situ forming gas (50%N₂+50%H₂) plasma before depositing

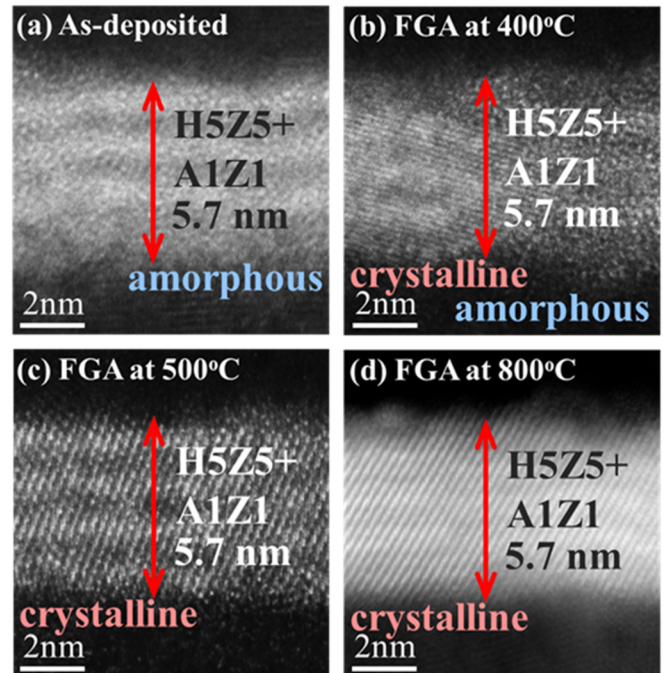


FIGURE 2. High-resolution Z-contrast images of films (a) as-deposited (amorphous), (b) FGA at 400°C (partially crystallized), (c) FGA at 500°C (highly crystallized), and (d) FGA at 800°C (highly crystallized).

oxide layers, hindering the oxygen diffusion between TiN and HZO, and suppressing the formation of TiO_xN_y and oxygen vacancies [10]. There was no plasma treatment on TiN top electrode, since the TiN top electrode was deposited after HZO layers.

The Hf_{0.5}Zr_{0.5}O₂ layer was deposited with 4 periods of H5Z5 (5 cycles of ZrO₂ and 5 cycles of HfO₂ per period) to form a superlattice structure that favored o-phase formation [11]. The thickness of the HZO layer was 5.7 nm. The Al₂O₃-ZrO₂ layer was fabricated with 3 periods of A1Z1 (1 cycle of ZrO₂ and 1 cycle of Al₂O₃ per period). The layered Al₂O₃-ZrO₂ structure was previously reported as a low leakage high-k dielectric material for DRAM applications [12], and it was used in our work as the leakage blocking layer during the C-V and P-V measurements. Circular Pt pads were crafted by lithography followed by Pt sputtering and lift-off process. Pt served as the etch-stop and top probe layer. Two steps of reactive ion etching (RIE) processes were used to etch away the top TiN electrode unprotected by Pt circles and to reveal the bottom probe layer. Finally, forming gas annealing (FGA) in 10%H₂+90%N₂ at 400°C, 500°C, and 800°C was used to crystallize the HZO layer.

III. RESULTS AND DISCUSSION

TEM images show that no crystal can be observed from the as-deposited film (Figure 2 (a)), both crystalline and amorphous portions exist after FGA at 400°C (Figure 2 (b)), and high-crystalline HZO layers are observed after FGA at 500°C and 800°C (Figure 2 (c) and Figure 2 (d)).

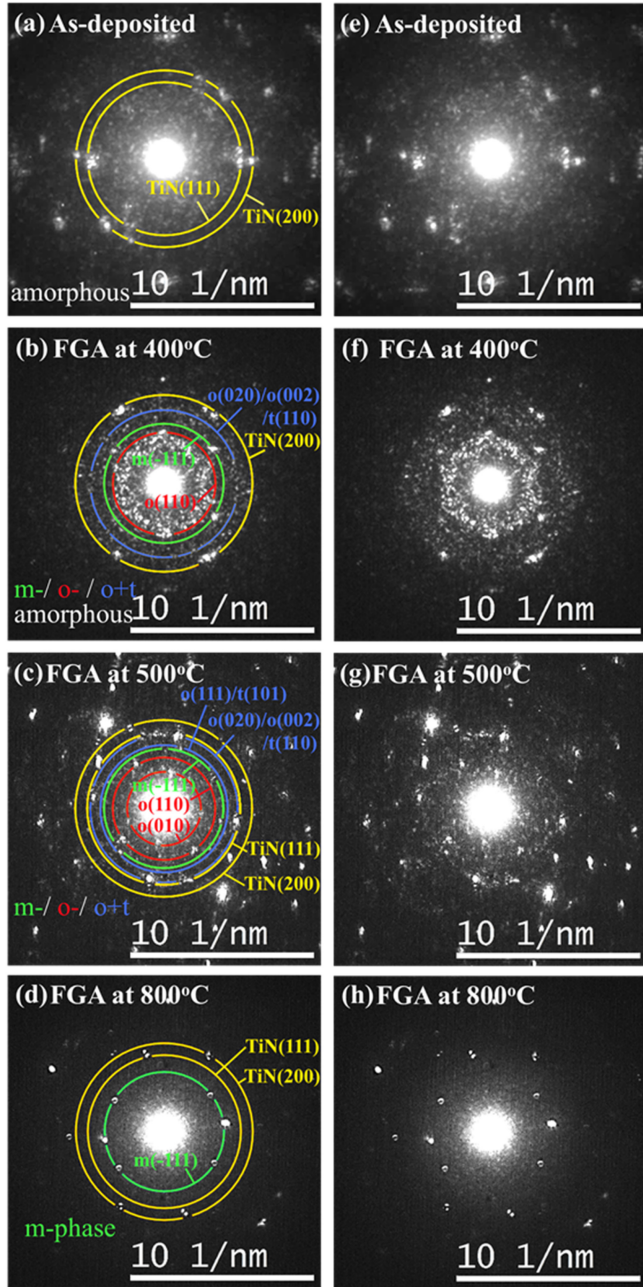


FIGURE 3. Nanobeam electron diffraction (NBD) images of films (a) as-deposited (amorphous,) (b) FGA at 400°C (with an o-phase red circle,) (c) FGA at 500°C (with o-phase red circles,) and (d) FGA at 800°C (with an m-phase green circle.) Note that (e, f, g, h) are the original NBD images without marking circles.

NBD was used to identify the HZO o-phase (Figure 3). Crystals with different lattice constants and orientations can be differentiated by the distance between the bright spots and the center [13], [14]. The distance is made clear by circles of different radii, and the existence of these bright spots is highlighted by the openings in the circles. As-deposited film (Figure 3 (a)) shows cloudiness near the center and no bright spot that matches HZO crystals, indicating that as-deposited film is amorphous. After FGA at 400°C (Figure 3 (b)),

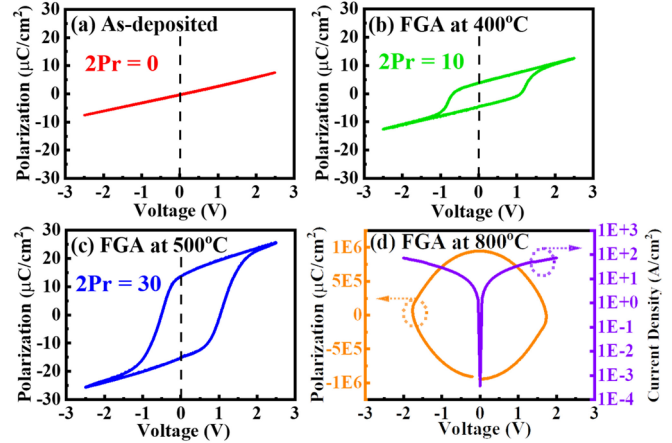


FIGURE 4. The P-V curves of MIM/MFM capacitors (a) as-deposited (dielectric behavior,) (b) FGA at 400°C (ferroelectric behavior,) (c) FGA at 500°C (ferroelectric behavior,) (d) FGA at 800°C (orange curve for polarization, and purple curve for leakage current density.).

some cloudiness can still be seen, showing that a portion of the HZO layer is still amorphous, while bright spots near the center form a circle matching the reference data for o-phase (110) lattice plane [14], indicating the existence of the o-phase crystal. The sole existence of t-phase cannot be identified by the o(020)/ o(002)/ t(110) spots that correlate to o-/ t-phase mix peak in GIXRD [15], [16] since the lattice constant of HZO t-phase and o-phase are very similar. The same analysis can also be applied to film FGA at 500°C (Figure 3 (c)). The cloudiness caused by amorphous HZO has been greatly reduced, showing high HZO crystallinity. A new red circle of o(010) is observed after FGA at 500°C, and the o(110) circle becomes brighter compared to o(110) circle from the film FGA at 400°C, indicating the amount of o-phase in film FGA at 500°C is higher than that of film FGA at 400°C. After FGA at 800°C (Figure 3 (d)) only m(-111) is observable. The disappearance of o-phase and t-phase bright spots is due to the metastable o-phase and t-phase transforming into the thermodynamically stable m-phase during FGA at 800°C [9]. The high-resolution Z-contrast TEM images and NBD images are obtained with Talos F200XG2 by Thermo Fisher Scientific. The electrons are emitted by field emission gun, and accelerated by 200kV accelerating voltage. The tilt angle of sample is $\pm 30^\circ$, the spot size of electron beam is 1.5nm, and the resulted resolution is 0.16nm.

To further understand the phase composition of the HZO layer, electric properties, including P-V (Figure 4) and C-V (Figure 5), were analyzed. After setting one probe on Pt top probe layer and one on Pt bottom probe layer, the C-V measurement was carried out using Keysight B1500A semiconductor device parameter analyzer for C-V measurement, and the P-V measurement was carried out using Radian Premier II Ferroelectric Tester. The measurement frequency for C-V measurement is 100kHz, and the measurement frequency for P-V measurement is 1kHz. The

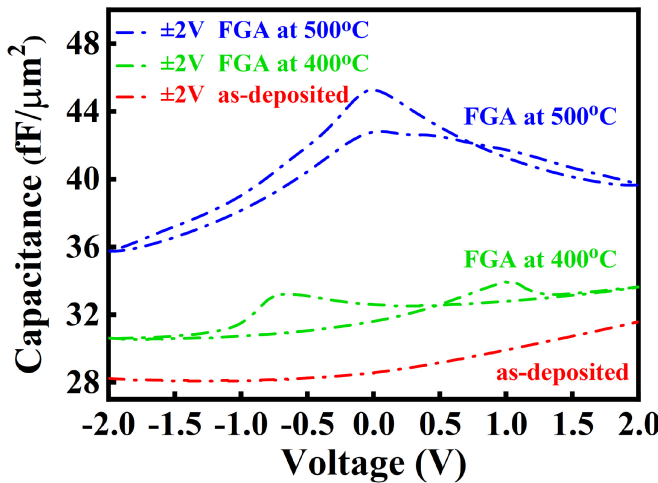


FIGURE 5. The C-V curves of MIM/MFM capacitors FGA at 500°C (ferroelectric behavior,) FGA at 400°C (ferroelectric behavior,) and as-deposited (dielectric behavior).

as-deposited film shows dielectric behavior with $2P_r$ equal to 0 (Figure 4 (a)). Both FGA at 400°C (Figure 4 (b)) and 500°C (Figure 4 (c)) films show a hysteresis loop confirming the existence of ferroelectric o-phase. $2P_r$ is $10\mu\text{C}/\text{cm}^2$ and $30\mu\text{C}/\text{cm}^2$ for films FGA at 400°C and 500°C, respectively. The increment in $2P_r$ comes from the increased crystallinity after annealing at 500°C as more amorphous HZO crystallized into the o-phase crystal. The measured polarization of FGA at 800°C film (Figure 4 (d)) is much higher than that of the 400°C/500°C annealed films due to leakage current, not ferroelectricity [17]. As we raise the annealing temperature to 800°C, the high thermal budget induces excess grain growth which enlarges the grain boundary to become major leaking paths [18]. The high leakage current density is shown in the purple curve (Figure 4 (d)). During the P-V measurement, an external voltage is applied to the capacitor that changes the polarization of the HZO film. The shifting of polarization will then change the charge on the electrodes required for charge neutralization, causing a current integrated by the tester and interpreted as polarization. Since the process measures the current flowing from the capacitor, it is also affected by the leakage current. For the orange curve in (Figure 4 (d)), the slope around 0V is very small, while the slope around $\pm 2\text{V}$ is very high due to the effects of leakage current, forming a circle-like trace.

The C-V curve can also identify ferroelectricity (Figure 5). The as-deposited film doesn't measure any hysteresis even with $\pm 2\text{V}$ sweep, showing dielectric behavior. FGA at 400°C and 500°C films show ferroelectric behavior which is indicated by the two peaks in the capacitance hysteresis loop [19]. Due to the plasma treatment performed on TiN bottom electrode but not TiN top electrode, the electrodes of the film is not symmetric, causing the asymmetric C-V curves.

TABLE 1. Parameters for calculating free energy.

HZO Phases	Bulk Energy (U_i) (eV/nm ³)	Entropy (S_i) (eV/nm ³ •K)	α -HZO (σ_i) (eV/nm ²)	TiN(100) (δ_i) (eV/nm ²)	Total Interfacial Energy (Γ_i) (eV/nm ³)
m-phase	0	0	9.40	20.25	10.52-10.24
o-phase	1.53	9.25E-5	7.33	18.94	9.31-9.09
t-phase	3.40	1.07E-3	5.14	18.79	8.46-8.30

HZO crystal structures, thermodynamic stability, and phase formation are heavily influenced by composition and grain size. High Zr concentration favors t-phase, not m-phase [20]. HZO grains grow in a columnar manner. The average grain size of the HZO crystal is similar to the thickness of the HZO layer [21] and larger grains favor m-phase formation [22], [23]. In our work, the calculated free energies by the DFT are used to estimate the relative free energy of phases at different temperatures [24], [25]. By thermodynamics, Gibbs free energy of a given system is calculated by

$$G_i = U_i - TS_i + \Gamma_i. \quad (1)$$

U , S , and Γ are bulk energy, entropy, and interfacial energy, respectively. Index i could be o-phase, t-phase, or m-phase. In the DFT simulation to calculate bulk energy, we used the Perdew–Burke–Ernzerhof exchange correlation function [26] as code to simulate a crystal structure consist of 4 Hf atoms, 4 Zr atoms, and 16 O atoms. 6% oxygen vacancies are in the lattice, and then we repeat the simulation for 100 times to find the average bulk energy. The entropy is taken from [27]. Interfacial energy of different phases are estimated by the DFT with

$$\Gamma_i = \frac{2\pi(r^2 \times \sigma_i + rd \times \delta_i)}{\pi r^2 d}, \quad (2)$$

considering cylindrical grain. The value of σ_i is estimated by simulating the interfacial energy between m-/ o- t-phase and amorphous HZO, and the value of δ_i is estimated by simulating the interfacial energy between m-/ o- t-phase and TiN(100) crystals. The values of σ_i and δ_i are taken from [22]. Thickness of the HZO film (d) is extracted from TEM images and set at 5.7nm, and the grain radius of the HZO crystals (r) is set at 5.5–6nm. The calculated Γ_i (Table 1) is $10.52\text{eV}/\text{nm}^3$ – $10.24\text{ eV}/\text{nm}^3$ for m-phase, $9.31\text{eV}/\text{nm}^3$ – $9.09\text{ eV}/\text{nm}^3$ for o-phase, and $8.46\text{eV}/\text{nm}^3$ – $8.30\text{ eV}/\text{nm}^3$ for t-phase [28], [29]. Referring the free energy of m-phase, the relative free energy of t-phase decreases drastically at increasing temperature, while the relative free energy of o-phase is almost independent of temperature (Figure 6). Reportedly previously, with grain boundary and interfacial energies both assumed to be 1/3 of the free surface energy, o-phase was more stable than t-phase when the temperature was lower than $\sim 250^\circ\text{C}$, and o-phase formation only happened during the cooling step [9]. After considering interfacial energies based on the DFT, schematic landscapes of free energy during the annealing and cooling process at different temperatures are drawn in this work

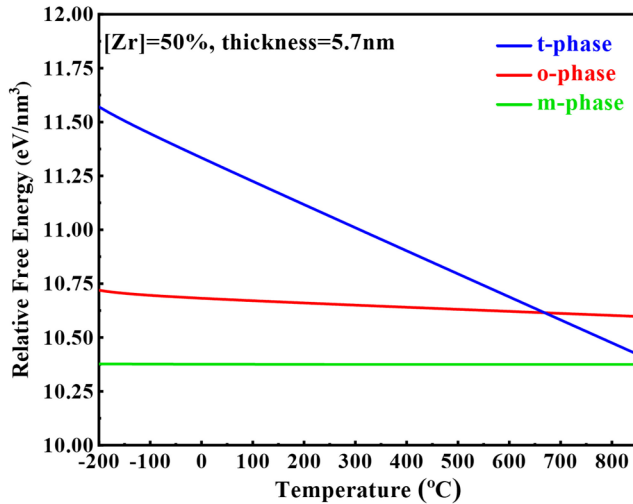


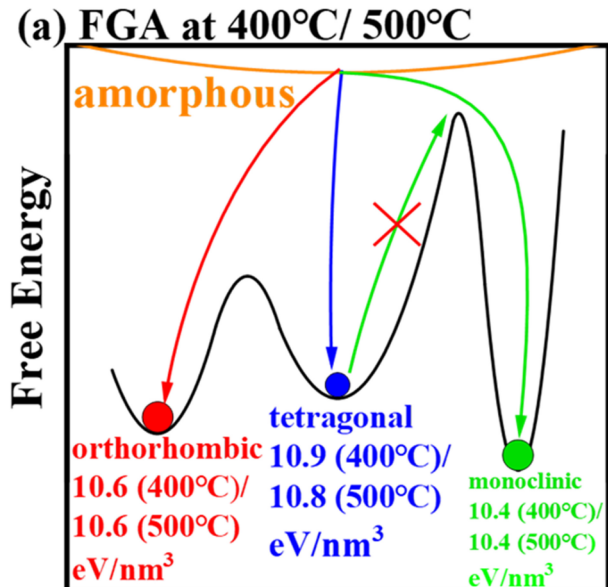
FIGURE 6. Relative free energy for m-/ o-/ t- phases at different temperatures.

TABLE 2. Lattice constants, angles, and volumes of HZO m-/ o-/ t- phase lattice cell.

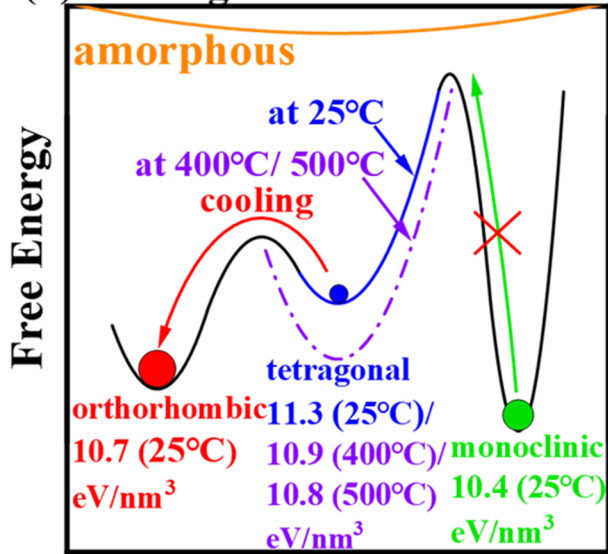
HZO	a (Å)	b (Å)	c (Å)	$\angle bc$	V (Å³)
m-phase	5.22	5.17	5.35	80.3	142
o-phase	5.29	5.07	5.10	90.0	137
t-phase	5.24	5.10	5.10	90.0	136

(Figure 7 and Figure 8). The activation barrier between o-phase and t-phase is low ($22\sim31\text{meV}/\text{formula unit}$), and the activation barrier between t-phase and m-phase is very high ($\sim315\text{meV}/\text{formula unit}$) as previously reported [23]. To compare the reported activation energy with our DFT results, lattice constants, angles, and volumes of HZO m-/ o-/ t- phase lattice cells (Table 2) were calculated. For HZO crystals, there are four formula units of atoms in one conventional lattice cell, and lattice cell volumes during phase transitions were assumed to be the average of the associated phases. The resulting activation barrier between o-phase and t-phase is $\sim0.788\text{eV}/\text{nm}^3$, and the activation barrier between t-phase and m-phase is $\sim9.03\text{eV}/\text{nm}^3$. Note that the free energy diagrams (Figure 7 and Figure 8) are purely schematic, and the activation barriers are not proportionally graphed. Since the activation barrier between t-phase and m-phase ($\sim9.03\text{eV}/\text{nm}^3$) is so much higher than activation barrier between o-phase and t-phase ($\sim0.788\text{eV}/\text{nm}^3$), the difference of Gibbs free energy between t-phase and o-phase ($\sim1.6\text{ eV}/\text{nm}^3$ at room temperature, $\sim0.2\text{ eV}/\text{nm}^3$ at 400°C , $\sim0.1\text{ eV}/\text{nm}^3$ at 500°C , and $\sim-0.2\text{ eV}/\text{nm}^3$ at 800°C), and the difference of Gibbs free energy between t-phase and m-phase ($\sim1.9\text{ eV}/\text{nm}^3$ at room temperature, $\sim0.5\text{ eV}/\text{nm}^3$ at 400°C , $\sim0.4\text{ eV}/\text{nm}^3$ at 500°C , and $\sim0.1\text{ eV}/\text{nm}^3$ at 800°C), a free energy diagram with proportionally scaled activation barriers cannot convey our ideas clearly.

During the annealing step, amorphous HZO crystallizes into the o-phase, t-phase, and m-phase crystals (Figure 7



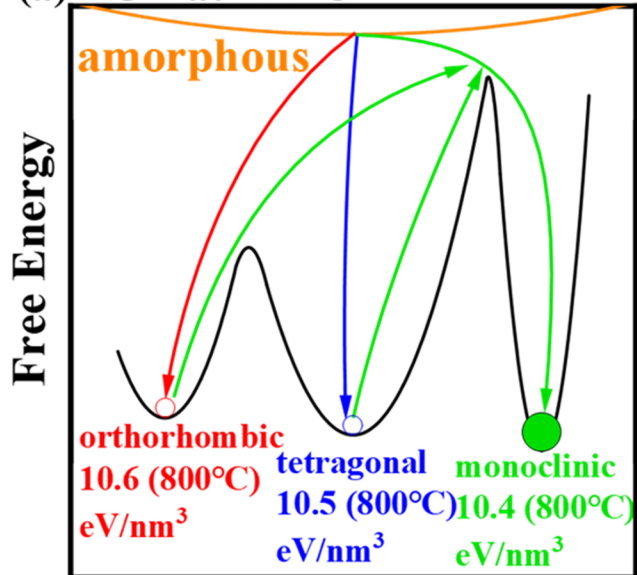
(a) FGA at 400°C/ 500°C



(b) Cooling from 400°C/ 500°C

(a) and Figure 8 (a)). During FGA at 400°C and 500°C (Figure 7 (a)), metastable o-phase and t-phase don't have enough thermal energy to cross the activation barrier between o-/ t-phase and m-phase. Therefore, metastable o-/ t-phase don't transform into stable m-phase. During cooling from $400^\circ\text{C}/ 500^\circ\text{C}$, t-phase transforms into o-phase (Figure 7 (b)) [28] since the relative free energy of t-phase increases and the barrier height from t-phase to o-phase decreases, similar to the cryogenic temperature [29]. During FGA at 800°C , metastable o-phase and t-phase possess enough energy to transform into stable m-phase (Figure 8 (a)). In contrast, m-phase cannot transform back into o-phase and t-phase during cooling (Figure 8 (b)) since m-phase is

(a) FGA at 800°C



(b) Cooling from 800°C

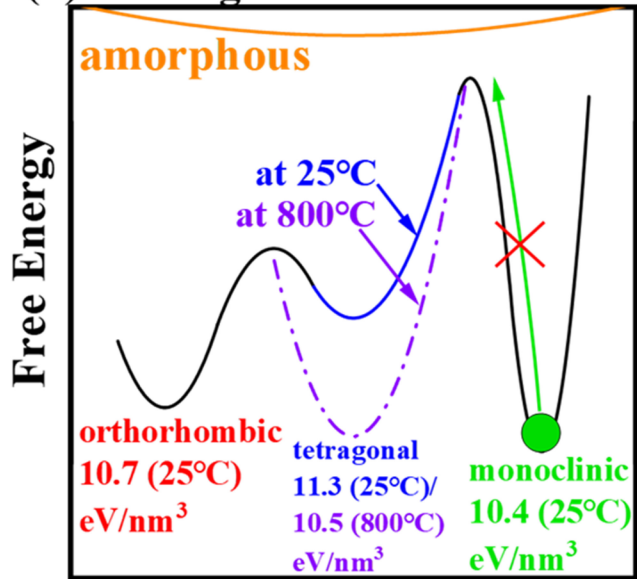


FIGURE 8. (a) Schematic diagram of free energy under 800°C. (b) Schematic diagram of free energy when cooling from 800°C. The size of the circles indicates the relative portion of every phase.

the stable phase with the lowest Gibbs free energy from 800°C to room temperature [30].

IV. CONCLUSION

In this work, phase development of HZO superlattice layer with various annealing conditions has been investigated experimentally and theoretically. Amorphous HZO crystallizes into the ferroelectric o-phase crystals during the annealing step (400°C/ 500°C), and t-phase transforms into o-phase during the cooling step. Annealing at 500°C instead of 400°C increases the crystallinity of the HZO

layer, achieving higher amount of o-phase and higher $2P_r$. Annealing at 800°C will provide sufficient thermal energy to overcome the activation barrier, transforming the metastable ferroelectric o-phase crystal into the stable dielectric m-phase crystal.

REFERENCES

- [1] T. Mittmann, M. Materano, S.-C. Chang, I. Karpov, T. Mikolajick, and U. Schroeder, "Impact of oxygen vacancy content in ferroelectric HZO films on the device performance," in *Proc. IEEE Int. Electr. Devices Meet. (IEDM)*, San Francisco, CA, USA, 2020, pp. 18.4.1–18.4.4, doi: [10.1109/IEDM13553.2020.9372097](https://doi.org/10.1109/IEDM13553.2020.9372097).
- [2] J. Lyu, T. Song, I. Fina, and F. Sanchez, "High polarization, endurance and retention in sub-5 nm $\text{Hf}_{0.5}\text{Zr}_{0.5}\text{O}_2$ films," *Nanoscale*, vol. 12, no. 20, pp. 11280–11287, 2020, doi: [10.1039/D0NR02204G](https://doi.org/10.1039/D0NR02204G).
- [3] J. Okuno et al., "Demonstration of fatigue and recovery phenomena in $\text{Hf}_{0.5}\text{Zr}_{0.5}\text{O}_2$ -based 1T1C FeRAM memory arrays," in *Proc. 6th IEEE Electr. Devices Technol. & Manuf. Conf. (EDTM)*, Oita, Japan, 2022, pp. 64–66, doi: [10.1109/EDTM53872.2022.9797943](https://doi.org/10.1109/EDTM53872.2022.9797943).
- [4] M. Saitoh et al., "HfO₂-based FeFET and FTJ for ferroelectric-memory centric 3D LSI towards low-power and high-density storage and AI applications," in *Proc. IEEE Int. Electr. Devices Meet. (IEDM)*, San Francisco, CA, USA, 2020, pp. 18.1.1–18.1.4, doi: [10.1109/IEDM13553.2020.9372106](https://doi.org/10.1109/IEDM13553.2020.9372106).
- [5] Y.-S. Kuo, S.-Y. Lee, C.-C. Lee, S.-W. Li, and T.-S. Chao, "CMOS-compatible fabrication of low-power ferroelectric tunnel junction for neural network applications," *IEEE Trans. Electr. Devices*, vol. 68, no. 2, pp. 879–884, Feb. 2021, doi: [10.1109/TED.2020.3045955](https://doi.org/10.1109/TED.2020.3045955).
- [6] H. Chen et al., "HfO₂-based ferroelectrics: From enhancing performance, material design, to applications," *Appl. Phys. Rev.*, vol. 9, no. 1, 2022, Art. no. 011307, doi: [10.1063/5.0066607](https://doi.org/10.1063/5.0066607).
- [7] P. Fan et al., "Origin of the intrinsic ferroelectricity of HfO₂ from ab initio molecular dynamics," *J. Phys. Chem. C*, vol. 123, no. 35, pp. 21743–21750, 2019, doi: [10.1021/acs.jpcc.9b04106](https://doi.org/10.1021/acs.jpcc.9b04106).
- [8] S. S. Cheema et al., "Enhanced ferroelectricity in ultrathin films grown directly on silicon," *Nature*, vol. 580, pp. 478–482, Apr. 2020, doi: [10.1038/s41586-020-2208-x](https://doi.org/10.1038/s41586-020-2208-x).
- [9] M. H. Park, Y. H. Lee, T. Mikolajick, U. Schroeder, and C. S. Hwang, "Thermodynamic and kinetic origins of ferroelectricity in fluoride structure oxides," *Adv. Electron. Mater.*, vol. 5, no. 3, 2019, Art. no. 1800522, doi: [10.1002aelm.201800522](https://doi.org/10.1002aelm.201800522).
- [10] Y. J. Lin, C. Y. Teng, C. Hu, C. J. Su, and Y. C. Yseng, "Impacts of surface nitridation on crystalline ferroelectric phase of $\text{Hf}_{1-x}\text{Zr}_x\text{O}_2$ and ferroelectric FET performance," *Appl. Phys. Lett.*, vol. 119, no. 19, Art. no. 192102, 2021, doi: [10.1063/5.0062475](https://doi.org/10.1063/5.0062475).
- [11] Z. Zhao et al., "Engineering $\text{Hf}_{0.5}\text{Zr}_{0.5}\text{O}_2$ ferroelectric/antiferroelectric phases with oxygen vacancy and interface energy achieving high remanent polarization and dielectric constants," *IEEE Electr. Device Lett.*, vol. 43, no. 4, pp. 553–556, Apr. 2022, doi: [10.1109/LED.2022.3149309](https://doi.org/10.1109/LED.2022.3149309).
- [12] H. J. Cho et al., "New TIT capacitor with $\text{ZrO}_2/\text{Al}_2\text{O}_3/\text{ZrO}_2$ dielectrics for 60nm and below DRAMs," in *Proc. Eur. Solid-State Device Res. Conf.*, 2006, pp. 146–149, doi: [10.1109/ESSDER.2006.307659](https://doi.org/10.1109/ESSDER.2006.307659).
- [13] J. Bouaziz, P. Rojo Romeo, N. Baboux, R. Negrea, L. Pintilie, and B. Vilquin, "Dramatic impact of pressure and annealing temperature on the properties of sputtered ferroelectric HZO layers," *APL Materials*, vol. 7, no. 8, 2019, Art. no. 081109, doi: [10.1063/1.5110894](https://doi.org/10.1063/1.5110894).
- [14] A. Chouprik et al., "Wake-Up in a $\text{Hf}_{0.5}\text{Zr}_{0.5}\text{O}_2$ film: A cycle-by-cycle emergence of the remnant polarization via the domain depinning and the vanishing of the anomalous polarization switching," *ACS Appl. Electron. Mater.*, vol. 1, no. 3, pp. 275–287, 2019, doi: [10.1021/acsaelm.8b00046](https://doi.org/10.1021/acsaelm.8b00046).
- [15] Y. Zheng et al., "In-situ atomic visualization of structural transformation in $\text{Hf}_{0.5}\text{Zr}_{0.5}\text{O}_2$ ferroelectric thin film: From nonpolar tetragonal phase to polar orthorhombic phase," in *Proc. Symp. VLSI Technol.*, Kyoto, Japan, 2021, pp. 1–2.
- [16] M. H. Park et al., "Origin of temperature-dependent ferroelectricity in Si-Doped HfO₂," *Adv. Electron. Mater.*, vol. 4, no. 4, 2018, Art. no. 1700489, doi: [10.1002aelm.201700489](https://doi.org/10.1002aelm.201700489).

- [17] M. H. Lee et al., "Ferroelectricity of HfZrO_2 in energy landscape with surface potential gain for low-power steep-slope transistors," *IEEE J. Electr. Devices Soc.*, vol. 3, no. 4, pp. 377–381, Jul. 2015, doi: [10.1109/JEDS.2015.2435492](https://doi.org/10.1109/JEDS.2015.2435492).
- [18] S. Kim, S. H. Lee, M. J. Kim, W. S. Hwang, H. S. Jin, and B. J. Cho, "Method to achieve the morphotropic phase boundary in $\text{Hf}_x\text{Zr}_{1-x}\text{O}_2$ by electric field cycling for DRAM cell capacitor applications," *IEEE Electron Device Lett.*, vol. 42, no. 4, pp. 517–520, 2021, doi: [10.1109/LED.2021.3059901](https://doi.org/10.1109/LED.2021.3059901).
- [19] M. H. Lee et al., "Steep slope and near non-hysteresis of FETs with antiferroelectric-like HfZrO for low-power electronics," *IEEE Electr. Device Lett.*, vol. 36, no. 4, pp. 294–296, Apr. 2015, doi: [10.1109/LED.2015.2402517](https://doi.org/10.1109/LED.2015.2402517).
- [20] J. Müller et al., "Ferroelectricity in simple binary ZrO_2 and HfO_2 ," *Nano Lett.*, vol. 12 no. 8, pp. 4318–4323, 2012, doi: [10.1021/nl302049](https://doi.org/10.1021/nl302049).
- [21] B. Y. Kim et al., "Study of ferroelectric characteristics of $\text{Hf}_{0.5}\text{Zr}_{0.5}\text{O}_2$ thin films grown on sputtered or atomic-layer-deposited TiN bottom electrodes," *Appl. Phys. Lett.*, vol. 117, no. 2, 2020, Art. no. 022902, doi: [10.1063/5.0011663](https://doi.org/10.1063/5.0011663).
- [22] Y.-T. Tang et al., "A comprehensive kinetical modeling of polymorphic phase distribution of ferroelectric-dielectrics and interfacial energy effects on negative capacitance FETs," in *Proc. Symp. VLSI Technol.*, Kyoto, Japan, 2019, pp. T222–T223, doi: [10.23919/VLSIT.2019.8776508](https://doi.org/10.23919/VLSIT.2019.8776508).
- [23] M. H. Park et al., "Understanding the formation of the metastable ferroelectric phase in Hafnia-Zirconia solid solution thin films," *Nanoscale*, vol. 10, no. 2, pp. 716–725, 2018, doi: [10.1039/C7NR06342C](https://doi.org/10.1039/C7NR06342C).
- [24] Y.-T. Tang et al., "A comprehensive study of polymorphic phase distribution of ferroelectric-dielectrics and interfacial layer effects on negative capacitance FETs for sub-5 nm node," in *Proc. IEEE Symp. VLSI Technol.*, Honolulu, HI, USA, 2018, pp. 45–46, doi: [10.1109/VLSIT.2018.8510696](https://doi.org/10.1109/VLSIT.2018.8510696).
- [25] Y.-W. Chen and C. W. Liu, "Boost of orthorhombic population with amorphous SiO_2 interfacial layer—A DFT study," *Semicond. Sci. Technol.*, vol. 37, no. 5, 2022, Art. no. 05LT01, doi: [10.1088/1361-6641/ac5a5e](https://doi.org/10.1088/1361-6641/ac5a5e).
- [26] J. P. Perdew, K. Burke, and M. Ernzerhof, "Generalized gradient approximation made simple," *Phys. Rev. Lett.*, vol. 78, p. 1396, Feb. 1997, doi: [10.1103/PhysRevLett.78.1396](https://doi.org/10.1103/PhysRevLett.78.1396).
- [27] R. Materlik, C. Künneth, and A. Kersch, "The origin of ferroelectricity in $\text{Hf}_{1-x}\text{Zr}_x\text{O}_2$: A computational investigation and a surface energy model," *J. Appl. Phys.*, vol. 117, no. 13, 2015, Art. no. 134109, doi: [10.1063/1.4916707](https://doi.org/10.1063/1.4916707).
- [28] Y. Zheng et al., "In-situ atomic-level observation of reversible first-order transition in $\text{Hf}_{0.5}\text{Zr}_{0.5}\text{O}_2$ ferroelectric film," in *Proc. Int. Electr. Devices Meeting (IEDM)*, San Francisco, CA, USA, 2022, pp. 6.3.1–6.3.4, doi: [10.1109/IEDM45625.2022.10019431](https://doi.org/10.1109/IEDM45625.2022.10019431).
- [29] Y. Xing et al., "Improved ferroelectricity in cryogenic phase transition of $\text{Hf}_{0.5}\text{Zr}_{0.5}\text{O}_2$," *IEEE J. Electr. Devices Soc.*, vol. 10, pp. 996–1002, 2022, doi: [10.1109/JEDS.2022.3218004](https://doi.org/10.1109/JEDS.2022.3218004).
- [30] U. Schroeder et al., "Temperature-dependent phase transitions in $\text{Hf}_x\text{Zr}_{1-x}\text{O}_2$ mixed oxides: Indications of a proper ferroelectric material," *Adv. Electron. Mater.*, vol. 8, no. 9, 2022, Art. no. 2200265, doi: [10.1002/aelm.202200265](https://doi.org/10.1002/aelm.202200265).